Rock and Soil Mechanics

Volume 41 | Issue 11 Article 6

4-8-2021

Study on tunnel water inrush mechanism and simulation of seepage failure process

Zong-qing ZHOU
State Key Laboratory of Mining Disaster Prevention and Control Co-founded by Shandong Province and the Ministry of Science and Technology, Shandong University of Science and Technology, Qingdao, Shandong 266590 China

Li-ping LI
Geotechnical and Structural Engineering Research Center, Shandong University, Jinan, Shandong 250061, China

Shao-shuai SHI
Geotechnical and Structural Engineering Research Center, Shandong University, Jinan, Shandong 250061, China

Cong LIU
School of Qilu Transportation, Shandong University, Jinan, Shandong 250002, China

See next page for additional authors

Custom Citation

ZHOU Zong-qing, LI Li-ping, SHI Shao-shuai, LIU Cong, GAO Cheng-lu, TU Wen-feng, WANG Mei-xia. Study on tunnel water inrush mechanism and simulation of seepage failure process[J]. Rock and Soil Mechanics, 2020, 41(11): 3621-3631.

Study on tunnel water inrush mechanism and simulation of seepage failure process

Authors

Zong-qing ZHOU, Li-ping LI, Shao-shuai SHI, Cong LIU, Cheng-lu GAO, Wen-feng TU, and Mei-xia WANG

Rock and Soil Mechanics 2020 41(11): 3621−3631 ISSN 1000−7598
https: //doi.org/10.16285/j.rsm.2020.5131 rocksoilmech.researchcommons.org/journal

Study on tunnel water inrush mechanism and simulation of seepage failure process

ZHOU Zong-qing[1, 2, 3, 4], LI Li-ping[1, 2], SHI Shao-shuai[1, 2], LIU Cong[1], GAO Cheng-lu[1], TU Wen-feng[1], WANG Mei-xia[1]

1. School of Qilu Transportation, Shandong University, Jinan, Shandong 250002, China

2. Geotechnical and Structural Engineering Research Center, Shandong University, Jinan, Shandong 250061, China

3. Key Laboratory of Geotechnical Mechanics and Engineering of Ministry of Water Resources, Yangtze River Scientific Research Institute, Wuhan, Hubei 430010 China

4. State Key Laboratory of Mining Disaster Prevention and Control Co-founded by Shandong Province and the Ministry of Science and Technology, Shandong University of Science and Technology, Qingdao, Shandong 266590 China

Abstract: In view of the two typical modes of water inrush disasters, progressive fracturing of rock mass and seepage failure of filling structure, the mechanism of progressive fracturing of rock mass under the combined effects of dynamic disturbance, excavation unloading and high water pressure is described. The seepage failure mechanism of the variable strength-variable permeability-variable viscosity of the filling structure under osmotic pressure is also expounded. For the variable viscosity mechanism of water inrush caused by seepage failure of filling structure, a qualitative simulation study on the effect of fluid viscosity on seepage failure mechanism is carried out using the DEM-CFD coupled simulation method. The effects of fluid viscosity on the average contact force, flow rate (flow velocity), porosity, particle migration process, migration trajectory and critical hydraulic gradient of the simulation model are analyzed. The results show that the critical hydraulic gradient of fluid with low viscosity is smaller than that with high viscosity. In other words, seepage failure of filling structure is more likely to occur under the action of fluid flow with low viscosity; the average contact force is especially sensitive to the response of critical value of the hydraulic gradient, however it is difficult to be accurately reflected by the flow rate. Considering only the variable viscosity mechanism of water inrush due to seepage failure (regardless of the effect of increasing permeability), as the viscous medium flows into water, the fluid viscosity would increase, but the flow velocity would decrease, and the combined action of these two changes would actually hinder the development of seepage failure process. Finally, the phenomenon of water inrush process in engineering scale is simulated using DEM-CFD method, and the formation and expansion process of the dominant channel of water inrush is reproduced. The problems of parameter selection and quantitative analysis are identified to realize the simulation of water inrush mechanism.

Keywords: water inrush disasters; mechanism; fluid viscosity; seepage failure; DEM-CFD; numerical simulation

1 Introduction

With the rapid development of China's infrastructure construction, major construction projects such as transportation, water conservancy and hydropower embraced new development opportunities that greatly promoted the construction of deep and long tunnels (cavers). In particular, with the expansion of the traffic road network to the western part of the country with lofty mountains, and the construction of water diversion projects such as the Han–Wei River water diversion, and the central Yunnan water diversion, hundreds of tunnels with depth over 1 km and length over 10 km have been developed. These projects have the remarkable characteristics of "significant buried depth, long distance, high in-situ stress, strong karst, high water pressure, complex structure, and frequent disasters".

For water conservancy and hydropower projects, the national planning focuses on the hydropower cascade development and the construction of water conservancy infrastructure in important river basins. With the development of many important river basins such as the Yarlung Zangbo River, Jinsha River, Lancang River, Yalong River, and Nu River, as well as the planning of cross-basin water transfer projects such as South-to-North Water Diversion, there are more than 20 world-class large-scale water conservancy and hydropower projects are under construction. For example, the total length of the water transmission line of the Central Yunnan Water Diversion Project exceeds 600 km and consists of more than 60 tunnels. The key control project Xianglushan Tunnel is about 60 km long and has a maximum buried depth of more than 1 km; the diversion tunnel of Qinling Water Diversion Project currently under construction has an approximate total length of 98.30 km, and the maximum buried depth exceeds 2 km.

For transportation engineering projects, the Chenglan Railway under construction can be used as an example.

Received: 9 January 2020 Revised: 13 April 2020
This work was supported by the National Natural Science Foundation of China (51709159, 51911530214), Shandong Provincial Key R&D Program of China (2019GSF111030), the CRSRI Open Research Program (CKWV2018468/KY) and the State Key Laboratory of Mining Disaster Prevention and Control Co-founded by Shandong Province and the Ministry of Science and Technology (MDPC201802).
First author: ZHOU Zong-qing, male, born in 1988, PhD, Assiciate Professor, PhD supervisor, focused in simulation analysis method of tunnel water inrush disaster mechanism and evolution process. E-mail: Zongqing.Zhou@sdu.edu.cn

Its tunnels occupy 67% of the total length of the railway line while traversing active fault zones and karst areas many times. The maximum buried depth of the tunnel is 1.9 km and the maximal long tunnel reaches 15 km. The Gaoligongshan Tunnel, a key control project of the Darui Railway, is currently the longest mountain railway tunnel in Asia with a total length of 34.5 km and a maximum buried depth of 1155 m. The soon-to-be constructed bridge and tunnel section from Ya'an to Linzhi of the Sichuan-Tibet Railway has a total length of 966 km. The section has a bridge-to-tunnel ratio of 96% with 72 tunnels having a total length of about 852 km that approximately accounts for 85% of the total length of the line, and the longest tunnel is 42.2 km.

Most of the above-mentioned tunnels are located in areas with high mountains and valleys. The situation of water inrush disasters caused by deep environment with groundwater abundance, high pressure or high ground stress is worsening while the chances of inducing major geological disasters such as water inrush, water resources depletion and surface collapse are increasing. The secondary environmental geological disasters pose a serious threat to the safety of tunnel construction, the safety of people's lives and property, and the preservation of the ecological environment. Thus, there are increasing needs and higher standards required for the prevention and control of water inrush disasters [1].

The prevention and control of tunnel water inrush disasters mainly include advanced prediction of adverse geology, disaster mechanism and evolution simulation, prediction, early warning and scientific decision-making, dynamic control and disaster prevention and so on. Among them, the scientific cognition of the water inrush catastrophe mechanism and the simulation of the evolution process are the theoretical basis of monitoring, early warning and control decision-making. A great amount of research has been carried out at home and abroad regarding areas, including the hydrogeological characteristics and conditions causing water inrush disaster[2], adverse geological geophysical detection theories and methods[3–6], water inrush prediction and early warning mechanism and control countermeasures [7–10], which are not expounded herein. Mainly based on the preliminary research of water inrush disaster, this paper expounds on the new understanding of the disaster mechanism, and uses the coupling method of discrete element (DEM)-computational fluid dynamics (CFD) to carry out the simulation analysis of seepage failure mechanism at sample scale and water inrush catastrophe process at engineering scale.

2 Disaster evolution mechanism of tunnel water inrush

Water inrush disaster refers to a kind of geological disaster, in which a large amount of water or mud-water mixture instantaneously bursts into the tunnel along the structural surfaces, such as rock joints, faults, karst pipelines, underground rivers and other adverse geological structures during the construction of tunnels and underground projects.

The tunnel water inrush disaster consists of three parts: disaster source, water inrush channel and anti-outburst structure. Disaster source is the primary factor and source of water inrush disaster, and it is the main research object of advanced tunnel geological forecast. The water inrush channel is the dominant migration channel for disaster sources that is usually formed by the destruction of the anti-outburst structure. The anti-outburst structure refers to the rock and soil body with the ability to prevent water inrush between the disaster source and the tunnel open surface. The failure mode of the anti-outburst structure and the formation process of the water inrush channel are the main research objects of the water inrush disaster mechanism, monitoring and early warning. According to the nature of the anti-outburst structure and its failure mode, the water inrush can be divided into progressive fracture type and filling body instability type.

2.1 Progressive fracture-type water inrush mechanism of anti-outburst rock

When there are large-scale water-conducting structures such as high-pressure water-rich caves in front of and around the tunnel, the fractured rock mass is an anti-outburst structure for water inrush disasters. This type of disaster is essentially the progress of crack generation and initiation, followed by gradual propagation and cut-through until rock mass ruptures to form a water inrush channel [11–14]. This process is promoted under the combined action of dynamic disturbance, excavation unloading and high osmotic pressure exerted on the primary joints, fissures or weak surfaces of the geological structure in the anti-outburst rock masses. Among them, dynamic disturbance and high osmotic pressure are the main external disturbance loads. The interaction between the three is shown in Fig. 1.

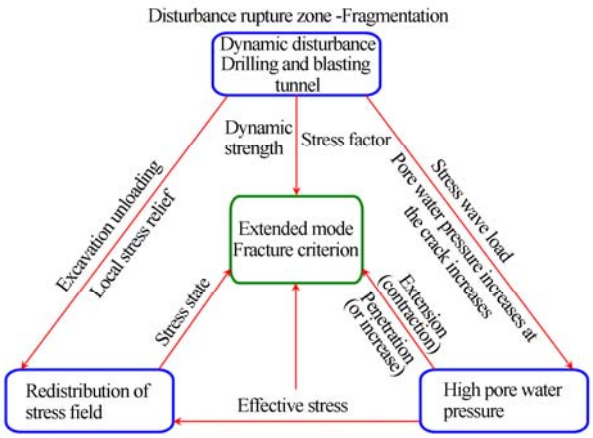

Fig. 1 Failure mechanism of rock mass under combined action of dynamic disturbance, unloading and high seepage pressure

First of all, blasting for excavation will instantly generate a huge amount of energy and the produced explosion gas will cause damage to the surrounding rock mass. At the same time, tunnel excavation results in the release of in-situ stress and the redistribution of the stress field, which adjusts the stress state around the

tip of the crack in the rock mass. Once the stress state changes, cracks will be initiated, followed by expansion and penetration. An interference fracture zone will be formed under the combined action of the two. The zone is mainly created by the compressive shear failure of the rock mass along the structural plane or due to the tensile failure along the radial direction of the blast hole; deep-buried tunnels are prone to the first scenario.

In addition, the load of stress wave generated by blasting is transmitted to the water-bearing cracks in the front that equivalently increases the pore water pressure at the cracks, causing changes of the effective stress and stress state at the crack (stress field redistribution also has an influence), resulting in the initiation, propagation and penetration of the water-bearing cracks. This also influences the propagation mode of the water-bearing cracks. After the crack propagates and coalesces to form a water passage, the pore water pressure in the cut-through crack will change. Under normal circumstances, the water pressure will decrease to a certain extent, but when the crack with low pore water pressure coalesces with the crack containing high porewater pressure, the water pressure in low pore water pressure crack may increase instantaneously[15], thereby further affecting the stress state and its propagation mode on the subsequent crack surface.

2.2 Mechanism of instability-type water inrush of filling body

The internal structure and spatial distribution have strongly anisotropy due to multi-stage tectonic movements in the formation process of geological structures such as wide fissures, fault fracture zones and karst pipelines, and its engineering hydrogeological conditions, structural development characteristics and cemented filling conditions are very complicated, which makes the instability water inrush mechanism and evolution process of the filling media extremely complicated. Take the fault fracture zone as an example. Firstly, the distribution characteristics of in-situ stress in the fault area are different because the fault attribute may be tensile or compressive fault or torsional fault; secondly, the fault fracture zone is often filled with a large number of media, and the filling media may be clay, fine sand or gravel, or a mixture of fault gouge, with different cementation characteristics and permeabilities. According to the cementation characteristics and permeability characteristics of the filling body, the water inrush disaster can be divided into three types: sliding instability type, seepage failure type and sand burst water inrush type [16–19].

2.2.1 Water inrush due to sliding instability

When the filling medium has high cementation strength, low permeability coefficient, and strong water blocking capacity, high-pressure water will seep along the side wall of the filling medium and rock mass, which weakens the side wall, and causes the entire filling to slide along the side wall, leading to the water inrush events.

2.2.2 Water inrush due to seepage damage

When the filling medium has low cementation strength and high permeability, high-pressure water will not only seep along the side wall, but also seep through the filling medium. As a result, the clay or fine particles of the filling medium are continuously lost, leading to reduction in the stability of the entire filling medium, finally a seepage-failure type water inrush disaster occurs.

Essentially, the water inrush induced by seepage failure of filling body is the process of seepage failure of filling bodies such as clay, mud sand and fault mud filled in faults, karst pipelines, highly weathered troughs and other bad geological structures under the action of high osmotic pressure. The penetration failure of the filling is a coupling process of varying strength, varying permeability, and varying viscosity, as shown in Fig. 2.

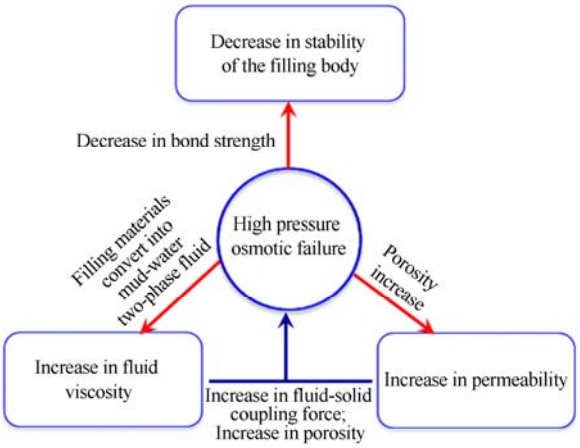

Fig. 2 Schematic diagram of seepage failure mechanism with variational strength, permeability and viscosity

Variable strength refers to the loss of viscous media inside the filling under the action of high osmotic water pressure, resulting in a decrease in the shear strength, which in turn changes the stability of the filling, causing it to be more prone to damage.

Variable viscosity refers to the increase of fluid viscosity after the viscous media flow into the water body. The fluid will thus change from pure ground-water (Newtonian fluid) to mud-water mixed fluid (non-Newtonian fluid), which increases the fluid's viscous drag force on the inside of the filling body.

Variable permeability means that the loss of viscous media will lead to an increase of porosity in the filling body and the increase of permeability in the whole disaster-causing structure. The increase of permeability will result in an increase in water flow velocity and fluid viscosity, which will increase the fluid–solid coupling force (viscous drag force caused by fluid flow and osmotic pressure caused by fluid pressure difference), and then increase the fluids scouring effect on the inner part of filling body and water inrush channel.

2.2.3 Water inrush due to sand burst

This type of water inrush disaster mainly occurs when the rock and soil around the tunnel are loose fine sand and gravel layers, such as water inrush from the sand layer at the Qingdao Metro. The layers of silty fine sand

will undergo damage similar to piping and flowing soil under the action of groundwater seepage. The specific failure mode mainly depends on the self-stability of the sand layer (i.e. movability and flowability of fine particles between the skeleton particles, which is closely related to the characteristics of the particle gradation curve).

Flow-soil type failure occurs when the sand is self-stable and piping type failure occurs when the sand is not self-stable, which consists of two stages: Suffusion stage and Suffosion stage. The first stage, Suffusion, is the movement and loss of fine particles between the interstices of the skeleton particles, resulting in increased local porosity and permeability (small increase), but the structure of the filling media remain undeformed. The second stage, Suffosion, refers to the continuous loss of fine particles, that is, the skeleton particles will move, which leads to the deformation and failure of the entire structure. At this time, there will be significant and rapid change on the permeability property [20–22].

3 Influence of fluid viscosity on seepage failure and water inrush mechanism

This section mainly adopts the coupling method of particle discrete element software (Particle Flow Code - PFC) and computational fluid dynamics (CFD) to carry out numerical simulation research on the influence of fluid viscosity on the mechanism of seepage failure. Since the quantitative relationship between loss of viscous media and shear strength, fluid viscosity and permeability of filling body has not been established yet, it is difficult to simulate the process of permeability, fluid property and flow state transition by the current calculation method because the fluid viscosity gradually increases with the continuous inflow of clay. To simplify the calculation, the numerical calculation process in this paper does not consider the gradual loss of the viscous media but assumes that the viscous media have been completely dissolved in the water and flows along (mud–water mixed flow). Then, the qualitative analysis of the influence of fluid viscosity on seepage failure mechanism of water inrush is performed. In the calculation, the PFC particle set is composed of non-viscous particles, only the viscosity of the fluid is changed, and the influence of the fluid viscosity on the process of internal particle migration and loss is analyzed.

3.1 DEM-CFD coupling calculation process

The DEM-CFD coupling calculation process is shown in Fig. 3. There is a significant number of related literatures regarding the DEM calculation principle and CFD calculation principle, and this article will not elaborate on them; the fluid-solid coupling force shown in the figure mainly refers to the drag force of the fluid on the particles. Generally, this value is obtained using a semi-empirical formula.

When the porosity is less than 0.8, the Ergun formula[23] is used:

$$f_{\mathrm{f}} = -\left(150\frac{1-n}{n_2\bar{d}^2}\upsilon\rho_{\mathrm{f}} + 1.75\frac{1}{n\bar{d}}\rho_{\mathrm{f}}\left|v_{\mathrm{rj}}\right|\right)v_{\mathrm{rj}}\frac{\pi}{6}d^3 \qquad (1)$$

where f_{f} is the drag force of the fluid on a single particle; n is the porosity; $\bar{d}$ is the average particle size of the particle set; ρ_{f} is the fluid density; υ is the dynamic viscosity of the fluid; v_{rj} is the relative velocity between the fluid and the solid particles; and d is the particle diameter.

When the porosity is greater than 0.8, the Wen and Yu formula [24] is used:

$$f_{\mathrm{f}} = -\frac{3}{4}\rho_{\mathrm{f}}C_{\mathrm{D}}\frac{n^{-2.7}}{\bar{d}}\left|v_{\mathrm{rj}}\right|v_{\mathrm{rj}}\frac{\pi}{6}d^3 \qquad (2)$$

where C_{D} is the drag coefficient, which is a function related to the Reynolds number Re [25].

$$\begin{aligned} C_{\mathrm{D}} &= \frac{24}{Re}\left(1+0.15Re^{0.687}\right),\ Re \leqslant 1\,000 \\ C_{\mathrm{D}} &= 0.44,\ Re \geqslant 1\,000 \end{aligned} \qquad (3)$$

The Reynolds number can be calculated by the following formula:

$$Re = \frac{n\left|v_{\mathrm{rj}}\right|}{\upsilon}\bar{d} \qquad (4)$$

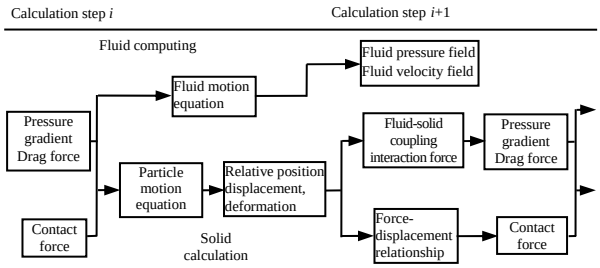

Fig. 3 DEM-CFD coupling simulation framework

3.2 DEM-CFD coupling calculation model

The discretization calculation model is shown in Fig. 4. The size of the model is 10 cm × 5 cm × 10 cm, and the particle set is composed of more than 25,000 particles; the radius expansion method is used to generate the required particles according to the particle grading curve shown in Fig.4. In the simulation process, linear contact stiffness model and sliding model are used. The particle-graded sample shown in Figure 4 does not have self-stability, that is, fine particles can move between the interstices created by coarse particles.

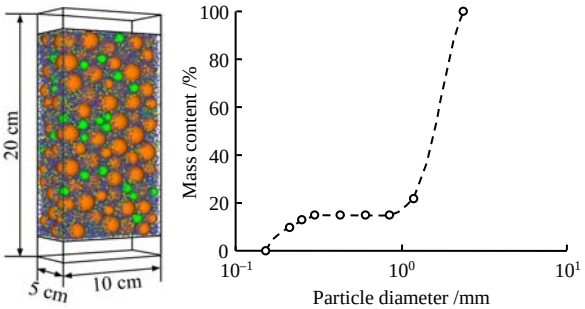

(a) PFC particle set (b) Particle size distribution curve

Fig. 4 Particle set and particle size distribution

The coarse grid fluid calculation scheme embedded in the PFC software has been mainly used for the flow simulation. This method solves the continuity equation of incompressible fluid and the Navier Stokes (N-S) equation to calculate the fluid pressure and velocity on each grid. The method of viscous damping is employed to dissipate contact energy, so that the model can reach a steady-state solution within a reasonable number of cycles. A total of 80 fluid grids are divided in the calculation model, and the size of each grid is 2.5 cm × 2.5 cm×2.5 cm. The upper boundary of the calculation model is set to adopt the Line wall to simulate the filter screen (0.8 mm spacing), while monitoring the flow rate, allowing fine particles to overflow from the above.

The upper boundary is the free boundary in the calculation, and the water pressure is always 0; the hydraulic gradient at the upper and lower ends of the sample is controlled by adjusting the size of the lower boundary water pressure; the other boundaries are impervious boundaries. Initially, water pressures are zero at both the upper and lower boundary, then, simulation of 0.2 s of real-physical time is performed to eliminate the unbalanced contact force between particles in order to reach a stable state. After that, the water pressure at the lower boundary is increased in a stepwise manner (a total of 9 steps), so that the hydraulic gradient at the upper and lower ends of the model are also increased step by step (0.2 each time) until the end of the calculation. Under each hydraulic gradient condition, the real physical time of 0.2 s is simulated, and the time step of the fluid calculation is 5.0×10^{-6} s.

The values of the meso-parameters are listed in Table 1. Among them, the particle density is the sand and gravel density; the fluid density is the groundwater density; the groundwater viscosity is taken as the basic viscosity, and the fluid viscosity is set to 0.2η , 1η , $\sqrt{5}\eta$ and 5η for comparison analysis during the calculation process. The values of the coefficient of friction between the particles and the wall, the normal stiffness of the particles, and the tangential stiffness are determined according to the values commonly used in the PFC manual and literature. The mechanical time step is automatically determined according to the parameters such as the radius, mass, and stiffness of the particles at the beginning of each cycle. The fluid time step is set to be about 100 times the mechanical time step.

Table 1 Meso-parameters of simulation model

Particle parameters				Time step / s		Wall parameters			Flow field parameters		
Friction coefficient	Density /(kg • m^{-3})	Normal stiffness /(N • m^{-1})	Tangential stiffness /(N • m^{-1})	Mechanics	Fluid	Friction coefficient	Normal stiffness /(N • m^{-1})	Tangential stiffness / (N • m^{-1})	Density /(kg • m^{-1})	Basic viscosity η / (Pa • s^{-1})	Grid size /mm
0.5	2 650	1×10^{6}	1×10^{6}	—	5×10^{-6}	0.5	1×10^{8}	1×10^{8}	1 000	0.001	2.5

3.3 Influence of fluid viscosity on average contact force

The change trend of the average contact force of the calculation model with the hydraulic gradient under different fluid viscosity conditions is presented in Fig. 5. The whole process can be divided into 4 stages:

(1) At this stage, the average contact force decreases rapidly. that the fine particles descend and deposit under the action of gravity, and contact with other particles, and the total contact quantity increases; the second reason is that the effective stress in the calculation model decreases after hydrostatic pressure is applied, which means that the total contact force is reduced.

Compared with low-viscosity conditions, the average contact force under high-viscosity conditions is larger, but its decreasing rate is smaller. This is mainly because the higher the fluid viscosity, the greater the viscous force of fluid on the particles, and the slower the deposition rate of fine particles; while under low viscosity conditions, more fine particles settle to the bottom, making the total number of particles in contact relatively large. Therefore, the average contact force is small.

(2) When the water pressure at the bottom of the model gradually increases, the average contact force slightly increases at first, then starts to decrease continuously. The reason for the slight increase is that the model reaches a stable state at the first stage, thus, the total contact force will increase slightly at the moment when the water pressure increases. The reason behind the continuous decrease is mainly due to that the force exerted by the fluid is insufficient to overcome the gravity exerted on the particles, leading to the particles continue to settle, and the total number of contacts is still increasing.

(3) When the hydraulic gradient reaches a certain value, the average contact force increases rapidly and changes frequently. At this stage, the drag force of the fluid on the particles is greater than the gravity of the particles, causing the particles to start moving upwards, and the total number of contacts therefore decreases; since the particles are in constant contact with other particles during the ascent process, resulting in the total number of contacts being always changing.

The critical hydraulic gradient under low viscosity conditions is smaller than that under high viscosity conditions, and the critical values of hydraulic gradient are 0.6, 0.8, 1.0, 1.0, respectively. This is mainly because the high-viscosity fluid experiences greater resistance to flow, and the flow velocity is slower under the same pressure; it also shows that the particles are easier to move under low-viscosity conditions.

(4) At this stage, the average contact force begins to decrease again, mainly due to the particles being interfered during the ascent process, and the fine particles regroup together, resulting in an increase in the total number of contacts.

If the water pressure continues to increase, the fine particles will continue to move upwards and eventually overflow the model from the upper end. When all the

fine particles are lost, the average contact force will remain constant, and there will be a slight increase when the water pressure increases. Due to the calculation time, this stage is not shown in the figure.

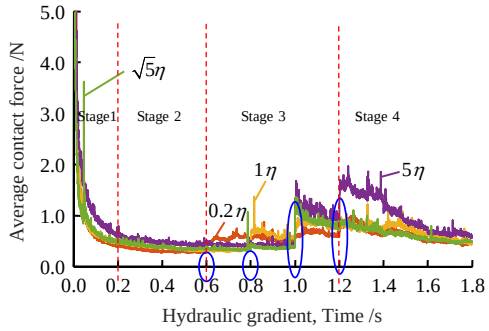

Fig. 5 Variation of mean contact force under different viscosities

3.4 Influence of fluid viscosity on flow rate (flow velocity)

The change trend of flow with hydraulic gradient is illustrated in Fig. 6. The stage of 0–0.2 s experiences the state of calculation equilibrium, then, the flow gradually increases as the hydraulic gradient increases. When the water pressure increases, the increase of the flow rate under low viscosity conditions is greater than that under high viscosity conditions. The reason is the same as mentioned above, the high-viscosity fluid experiences greater resistance. Therefore, the flow velocity under low viscosity conditions is larger than that under high viscosity conditions under the same hydraulic gradient circumstances.

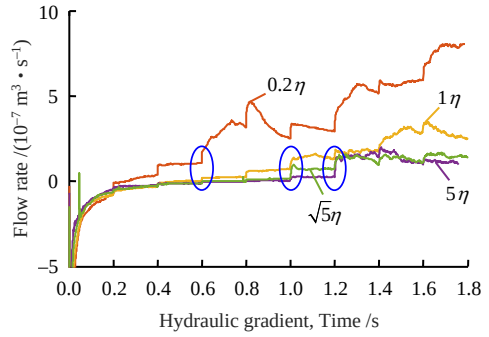

Fig. 6 Variation of flow rate under different viscosities

As the hydraulic gradient increases, the flow rate increases sharply and begins to fluctuate, and no longer maintains a relatively stable value, indicating that the fine particles have begun to move upwards under the action of the fluid, which means that the current hydraulic conditions have reached or exceeded the critical hydraulic gradient.

3.5 Influence of fluid viscosity on porosity

During the numerical simulation, the model was divided into 4 layers from top to bottom, and the porosity changes of each layer were monitored. The change trend of the average porosity of the upper three layers on the model with the hydraulic gradient is shown in Fig. 7.

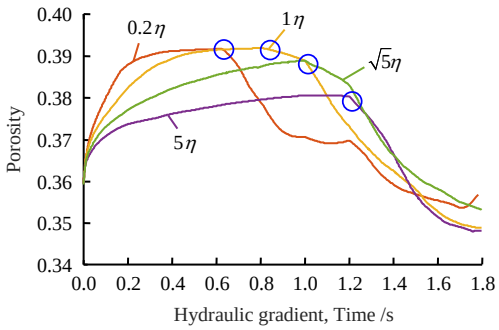

Fig. 7 Variation of porosity (upper three layers) under different viscosities

The porosity increases first, mainly because the fine particles move to the bottom of the model under the action of gravity; at this time, the porosity under low viscosity conditions is greater than the porosity under high viscosity conditions, mainly because the particles are easier to settle to the bottom of the model under low viscosity conditions.

When a certain hydraulic gradient is reached, the porosity begins to decrease as the fine particles begin to ascend under the action of fluid force. The critical hydraulic gradient under low viscosity conditions is smaller than that under high viscosity conditions.

3.6 Particle migration process

The migration process of particles under the condition of fluid viscosity of 1 was analyzed as a sample. The changes of porosity at each layer of the calculation model are shown in Fig. 8. Among them, 0 represents the porosity of the entire model, 1 represents the porosity of the top layer, 2 represents the porosity of the second layer, 3 represents the porosity of the third layer, and 4 represents the porosity of the bottom layer.

The total porosity of the model basically remains unchanged, indicating that the number of fine particles lost from the top of the model is very small, and has little effect on the porosity of the entire model. The occurrence of this phenomenon is mainly due to the short calculation time and limited particle movement distance, and the particles have not yet flowed out from the top; if the calculation time is long enough, fine particles will eventually overflow from the top, and the total porosity of the model will increase accordingly.

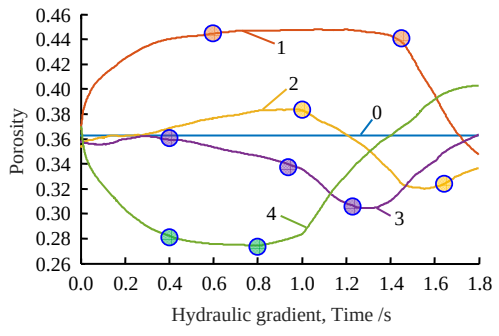

Fig. 8 Variation of porosity (each layer) under different viscosities

The total porosity of the model remains unchanged, but the porosity of each layer has been changing throughout the entire calculation time, indicating that the fine particles are constantly moving between the voids of the skeleton particles under the combined action of fluid force and gravity.

The porosity of the bottom layer shows a trend of rapid decrease at first, then towards stabilization, then rapid increase, and again towards stabilization. The rapid decrease is mainly due to the fact that the fine particles from the upper layers of the model continue to enter the bottom layer and stay in this layer (the bottom boundary restricts these particles from continuing to descend) ($t = 0 - 0.4$ s). When the voids in this layer are filled or blocked, the fine particles from upper layers are no longer able to flow to the bottom, the porosity therefore could remain at a relatively stable value ($t = 0.4 - 0.8$ s). When the hydraulic gradient is large enough, the fluid force overcomes gravity, leading to the particles flowing upwards and gradual increase of the porosity ($t = 0.8 - 1.6$ s). Finally, when all the fine particles enter the upper layers, the porosity begins to stabilize ($t =$ 1.6–1.8 s).

The porosity of the third layer presents with a trend of slow change, then gradual decrease, and then rapid increase. The slow change is due to the fact that while the fine particles of this layer continue to move down to the bottom layer, there is a continuous flow of fine particles entering this layer from the upper layer ($t =$ 0–0.4 s). When the porosity of the bottom layer stabilizes, the fine particles are no longer able to continue to move down, but there are still particles entering this layer from the above ($t = 0.4 - 0.8$ s), and the particles in the bottom layer also begin to gain access to this layer ($t =$ 0.8–1.2 s) under the action of the fluid, resulting in a gradual decrease in the porosity. When all the particles from the bottom layer flow into this layer while the fine particles of this layer continue to move into the upper layer, the porosity begins to increase ($t = 1.2 - 1.8$ s).

The porosity of the second layer shows a trend of slow increase, then gradual decrease, and then gradual increase. The slow increase is mainly due to the fact that the fine particles of this layer continue to move into the next layer ($t = 0 - 1.0$ s), but at the same time there is a continuous flow of fine particles entering this layer from the uppermost layer ($t = 0 - 0.6$ s), so the porosity increase rate is faster than that of the uppermost layer. When the particles of the next layer start to enter this layer under the force of the fluid, the porosity begins to decrease rapidly ($t = 1.0$–1.6 s). When all the fine particles of the next layer flow into the layer, the fine particles of this layer continue to move into the uppermost layer. Therefore, the porosity of this layer begins to increase ($t = 1.6$ to 1.8 s).

The porosity of the top layer presents with a trend of rapid increase at first, then stabilization, and then rapid decrease. The rapid increase is mainly due to the downward movement of fine particles (0–0.6 s) under the action of gravity; when all the fine particles move to the lower layer, the porosity reaches a relatively stable value (0.6–1.4 s). When the fine particles enter the layer under the force of fluid, the porosity begins to decrease rapidly (1.4–1.8 s).

The migration process of fine particles is shown in Fig. 9. The entire particle migration process is summarized as follows: when the hydrostatic pressure is applied or the fluid force is less than the buoyant weight of the particles, the fine particles in the calculation model descend and settle to the bottom of the model (0–1.8 s). When the fluid force is greater than the buoyant weight of the particles, the fine particles move upward from the bottom layer (0.8 s), and continue to enter the second layer (1.0 s), the third layer (1.2 s), and the top layer (1.4 s). Eventually, overflow from the top of the model.

3.7 Particle migration trajectory

By extending the function of the program, the tracking of the migration path of fine particle is realized. During the calculation, the migration paths of the two fine particles (particle IDs 12 516 and 18 818) at the center of the model were monitored, as shown in Fig. 10. Their migration paths are illustrated in Fig 11 and Fig. 12.

After the hydrostatic pressure is applied, the particles quickly settle down and deposit to the bottom of the model; when the hydraulic gradient is small and the effect of the fluid on the particles is less than that of the gravity, the particles still remain at the bottom. When the hydraulic gradient reaches a certain value, the particles start to move upwards, and eventually rest at a location and stop moving again. The migration path of the fine particles is rather random, and the migration direction is constantly changing. This is mainly caused by the constant contact with the skeleton particles during the movement of the fine particles and the resistance created by the skeleton particles.

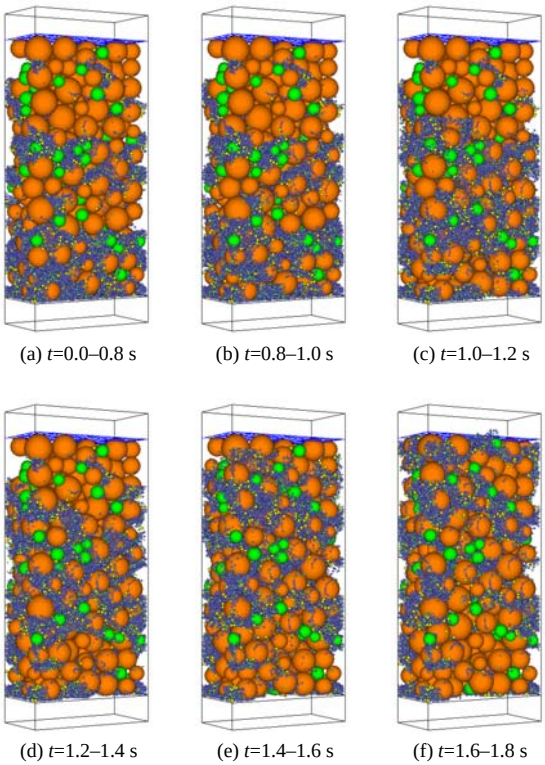

(a) t=0.0–0.8 s (b) t=0.8–1.0 s (c) t=1.0–1.2 s

(d) t=1.2–1.4 s (e) t=1.4–1.6 s (f) t=1.6–1.8 s

Fig. 9 Migration process of fine particles

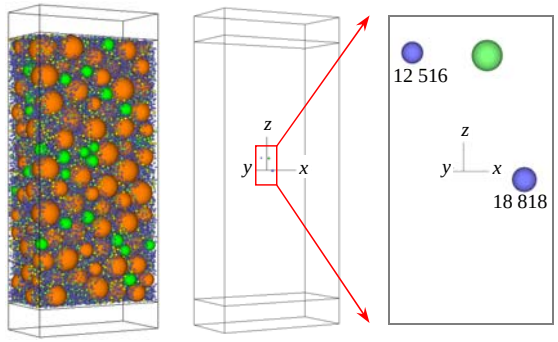

(a) PFC particle set (b) 监测颗粒所在位置

Fig. 10 Initial locations of monitored fine particles

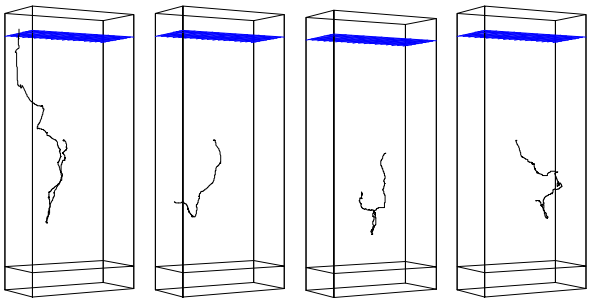

(a) 0.2η (b) 1η (c) $\sqrt{5}\ \eta$ (d) 5η

Fig. 11 Migration pathway of particle id=12 516

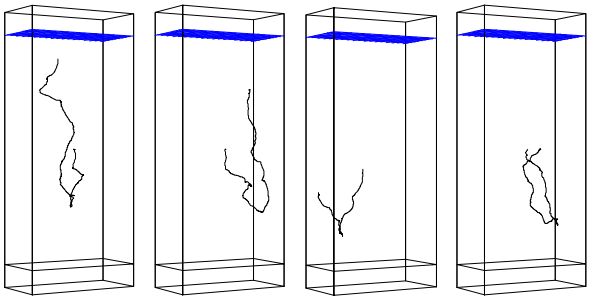

(a) 0.2η (b) 1η (c) $\sqrt{5}\ \eta$ (d) 5η

Fig. 12 Migration pathway of particle id=18 818 under different fluid viscosities

3.8 Critical hydraulic gradient

In the numerical calculation, the critical value of the hydraulic gradient at which the particles begin to move upward can be analyzed and be determined according to the change of the average contact force, flow rate, porosity and other information and video files (see Table 2).

Table 2 Responses of variables on critical hydraulic gradient

Viscosity	Average contact force	Flow rate	porosity
0.2η	0.6	0.6	0.6
1η	0.8	1.0	0.8
$\sqrt{5}\ \eta$	1.0	1.0	1.0
5η	1.0	1.2	1.2

For the four calculation conditions 0.2η, 1η, 5η, and 5η, the influence of fluid viscosity on the average contact force shows that the critical values of hydraulic gradient are 0.6, 0.8, 1.0, and 1.0 respectively; the influence of fluid viscosity on flow rate shows that the critical values of hydraulic gradient are 0.6, 1.0, 1.0, 1.2, respectively; and the influence of fluid viscosity on porosity shows that the critical values of hydraulic gradient are 0.6, 0.8, 1.0, 1.2, respectively. It means that the critical hydraulic gradient under low viscosity conditions is smaller than that under high viscosity conditions, but the critical hydraulic gradient values reflected by different monitoring information are different.

Combined with the video file generated in the numerical calculation, it is determined that the critical hydraulic gradients at which the particles at the very bottom layer start to move upward are 0.6, 0.8, 1.0, 1.0. Compared with the results above, it can be found that the average contact force is most sensitive to the change of the critical hydraulic gradient. However, critical values are difficult to be accurately reflected by the change of flow rate. The reason is that the flow rate only begins to fluctuate and significantly increase when a run-through seepage channel is about to form while the fine particles may already have begun to move just without the formation of any substantial channel.

It should be noted that the critical hydraulic gradients of 0.6, 0.8, 1.0, 1.0 here are an approximate values, because the hydraulic gradient increases by 0.2 each time. To obtain a more accurate hydraulic gradient, the water pressure should be increased by a smaller amount. For example, the calculation can be performed every time when the hydraulic gradient increases by 0.05.

4 Simulation of seepage failure and water inrush catastrophe process

4.1 Phenomenon simulation of water inrush catastrophe process

The water inrush and mud inrush disaster in the F2 fault zone of Yonglian Tunnel in Jiangxi Province was investigated as an example in this paper. A simulation-based analysis of the process of seepage failure and water inrush disaster was carried out. From July to October 2012, when the Yonglian Tunnel being excavated crossed the F2 fault zone, a total of 15 large-scale water and mud outbursts occurred. The mud outburst was 4.5× 10 m^3, while the collapsed surface area in the 200 m-high mountain top reached 2,000 m^2. The geological model of this section is shown in Fig. 13.

Based on the existing DEM-CFD calculation method, with the use of the PFC and EDEM software, PFC-CFD and EDEM-Fluent coupling calculation models for the water inrush of Yonglian Tunnel was established, which realistically reproduced the process of filling body seepage failure to water inrush disaster. The simulations of the phenomenon are shown in Figs. 14 and 15.

It can be observed from Figs. 14 and 15 that the development process of the seepage failure of the filling media and the dominant channel formation process are divided into three main stages (see Fig. 16). Since the hydraulic slope of the tunnel face is the largest, the permeation outlet is formed at the weakest filled region. After the formation of the outlet, the water flows to it while collecting and transferring the viscous media nearby, and the permeation channel forms an upward

trend (deflection to the direction where the equilibrium conditions are weakest); the permeation channel further develops upstream and gradually penetrates the upper water body, leading to the occurrence of water inrush disasters. At the same time, the water flow rate significantly increases, which has a powerful erosion effect on the media along both sides of the channel, resulting in erosion and expansion. In short, seepage failure is the decrease in the overall strength of the filling under the action of high-water pressure, which first leads to the failure at the permeation outlet and the upstream expansion of the permeation channel from the outlet along the direction with the weakest equilibrium condition. In addition, the scouring and expansion effects on the sidewall after the permeation channel being formed are also part of the process[7].

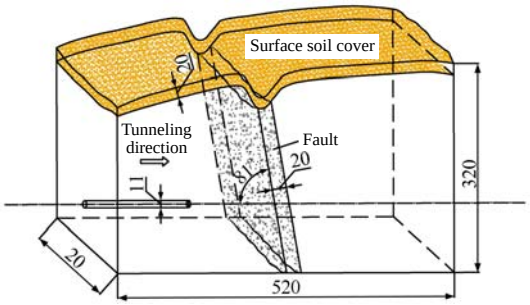

(a) Three-dimensional schematic

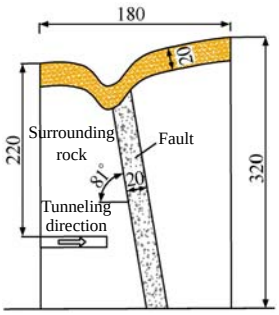

(b) Two-dimensional schematic

Fig. 13 Conceptual diagram of geological model (unit: m)

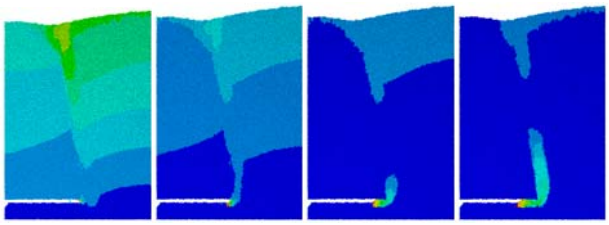

Fig. 14 PFC simulation result of water inrush process

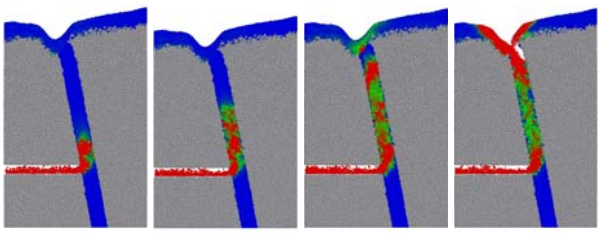

Fig. 15 EDEM simulation result of water inrush process

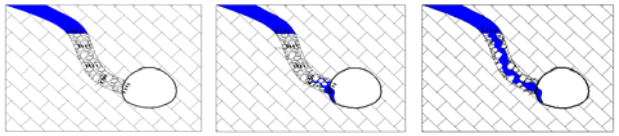

(a) Strength failure (b) Permeation outlet (c) Channel expansion

Fig. 16 Schematic diagram of horizontal expanding and longitudinal development process of water inrush channel

4.2 Discussion

As expounded in Section 3 and Section 4.1 of this paper, the coupling method of DEM and CFD can be used to simulate the seepage failure of the filling body at sample scale, as well as the simulation of the tunnel water inrush phenomenon at macro-scale or engineering scale.

In the sample-scale simulation, the particle size of the DEM can be set according to the particle gradation of the rock and soil, and the meso-parameters are determined according to the indoor test and calibration test, so as to realize the quantitative simulation and analysis of the seepage failure mechanism.

If the macro-scale simulation still uses the particle size of the same order of magnitude as the actual rock and soil (sample size), it will result in calculation amount far exceeding the hardware capacity of current computer. This means that the actual particle size of rock and soil and the meso-particle contact parameters calibrated through laboratory tests cannot be directly used for engineering scale calculations. Therefore, the macro-scale or engineering-scale water inrush simulation is currently only used for the description of the phenomenon instead of a quantitative analysis of the catastrophe mechanism.

In the macro-scale water inrush simulation described in Section 4.1, the particle size used is the value of the magnified particle size of the rock and soil mass that filled the fault. The magnification of the particle size and the increase of simulation scale will lead to a great difference in the quantitative selection of meso parameters between macro scale simulation and experimental scale simulation, and the multi-physical field information such as displacement, seepage obtained by the simulation is difficult to be compared and analyzed with the actual engineering scenarios. Therefore, one of the challenges facing further research in quantitative analysis of water inrush disaster mechanism is the consideration of particle scale effect and simulation scale effect, as well as the justification and confirmation of the selection of the contact parameters and conversion between different physical fields in the macro-scale simulation.

5 Conclusions and future prospective

(1) According to the different water-inrush prevention ability of the rock and soil body between the disaster source and the tunnel surface, the water inrush disaster is divided into two typical water inrush modes: the progressive failure of the anti-outburst rock and the instability of the filling body. The mechanism of rock mass fracture under the combined action of strong dynamic distur-

bance, excavation unloading and high water pressure is described in detail, as well as the seepage failure mechanism of "variable strength–variable permeability–variable viscosity" of the fillings under high osmotic pressure.

(2) Aiming at the variable viscosity mechanism of the seepage failure of the filling body, the DEM-CFD coupling method was used to carry out a qualitative simulation study of the influence of fluid viscosity on the seepage failure mechanism. Effect of the fluid viscosity on the average contact force, flow rate (flow velocity), porosity, particle migration process, migration trajectory and critical hydraulic gradient was analyzed. Calculation shows that the critical hydraulic gradient under low-viscosity conditions is smaller than that under high-viscosity conditions; the average contact force is most sensitive to the critical value of the hydraulic gradient while the flow rate is difficult to be used to accurately reflect this information.

(3) The critical hydraulic gradient under low-viscosity conditions is smaller than that under high-viscosity conditions. In other words, the fillings under low-viscosity conditions are more prone to seepage failure. The main reason is that the higher the fluid viscosity, the greater the resistance to fluid flow. Therefore, under the same hydraulic gradient conditions, the flow velocity under low viscosity conditions is larger than that under high viscosity conditions. This indicates that in the process of osmotic failure, as the viscous medium flows into the water body, although the viscosity of the fluid increases, the flow velocity of the fluid will decrease, and the combined action of the two will reduce the viscous drag force of the fluid flow on the filling body. Therefore, in terms of the variable viscosity mechanism alone (without considering the effect of increased permeability), the increase in viscosity hinders the development of the process of seepage failure.

(4) The DEM-CFD calculation method was used to conduct the simulation of water inrush disaster process at an engineering-scale and reproduces the formation and expansion process of inrush dominant channel. However, the quantitative simulation analysis of the disaster mechanism has yet not to be achieved with the simulation results having difficulties to be quantitatively compared with and analyzed against the actual engineering scenarios.

(5) The numerical calculation in this paper only was simplified to qualitatively explore the influence of fluid viscosity on the mechanism of seepage-failure water inrush without considering the evolution simulation of permeability; while seepage failure water inrush is a complex coupling process of "variable intensity, variable permeability, and variable viscosity". In order to realize the real simulation of the seepage field during the entire process, further research needs to be carried out targeting at the change law and simulation methods of permeability and viscosity with the loss of viscous medium, thus to reveal the influence of the combined action of the variable permeability and variable viscosity on seepage failure.

References

[1] QIAN Qi-hu. Challenges faced by underground projects construction safety and countermeasures[J]. Chinese Journal of Rock Mechanics and Engineering, 2012, 31(10): 1945–1956.

[2] LI Shu-cai, XU Zhen-hao, HUANG Xin, et al. Classification, geological identification, hazard mode and typical case studies of hazard-causing structures for water and mud inrush in tunnels[J]. Chinese Journal of Rock Mechanics and Engineering, 2018, 37(5): 1041–1069.

[3] LI S C, ZHOU Z Q, YE Z H, et al. Comprehensive geophysical prediction and treatment measures of karst caves in deep buried tunnel[J]. Journal of Applied Geophysics, 2015, 116(5): 247–257.

[4] LI Shu-cai, LIU Bin, SUN Huai-feng, et al. State of art and trend of advanced geological prediction in tunnel construction[J]. Chinese Journal of Rock Mechanics and Engineering, 2014, 33(6): 1090–1113.

[5] LI Shu-cai, LI Shu-chen, ZHANG Qing-song, et al. Forecast of karst-fractured groundwater and defective geological conditions[J]. Chinese Journal of Rock Mechanics and Engineering, 2007, 26(2): 217–225.

[6] LI Shu-cai, XUE Yi-guo, ZHANG Qing-song, et al. Key technology study on comprehensive prediction and early-warning of geological hazards during tunnel construction in high-risk karst areas[J]. Chinese Journal of Rock Mechanics and Engineering, 2008, 27(7): 1297–1307.

[7] LI S C, ZHOU Z Q, LI L P, et al. A new quantitative method for risk assessment of geological disasters in underground engineering: attribute interval evaluation theory (AIET)[J]. Tunnelling and Underground Space Technology, 2016, 53(3): 128–139.

[8] LI S C, ZHOU Z Q, LI L P, et al. Risk assessment of water inrush in karst tunnels based on attribute synthetic evaluation system[J]. Tunnelling and Underground Space Technology, 2013, 38(9): 50–58.

[9] LI Shu-cai, ZHOU Zonq-ging, LI Li-ping, et al. Risk evaluation theory and method of water inrush in karst tunnels and its applications[J]. Chinese Journal of Rock Mechanics and Engineering, 2013, 32(9):1858–1867.

[10] LI L P, LEI T, LI S C, et al. Dynamic risk assessment of water inrush in tunnelling and software development[J]. Geomechanics and Engineering, 2015, 9(1): 57–81.

[11] LI Shu-cai, WANG Kang, LI Li-ping, et al. Mechanical mechanism and development trend of water-inrush disaster in karst tunnels[J]. Chinese Journal of Theoretical and Applied Mechanics, 2017, 49(1): 22–30.

[12] WANG Yuan, LU Yu-guang, NI Xiao-dong, et al. Study on the mechanism of water inrush and mud in the process of excavation of deep tunnel[J].Journal of Hydraulic Engineering, 2011, 42(5): 595–601.

[13] LI Li-ping, LI Shu-cai, SHI Shao-shuai, et al. Multi-field coupling mechanism of seepage damage for the water inrush channel formation process of coal mine[J]. Journal of Mining & Safety Engineering, 2012, 29(2): 232–238.

[14] LI Li-ping, ZHU Yu-ze, ZHOU Zong-qing, et al. Calculation methods of rock thickness for preventing water inrush in tunnels and their applicability evaluation[J]. Rock and Soil Mechanics, 2020, 41(Suppl.1): 41–50, 170.

[15] CHEN Ming, LU Wen-bo, YAN Peng et al. Disturbance mechanism of blasting excavation to aquiferous rock crack propagation[J]. Rock and Soil Mechanics, 2014, 35(6): 1555–1560.

[16] LI Li-ping, LI Shu-cai, SHI Shao-shuai, et al. Water inrush mechanism study of fault activation induced by coupling effect of stress-seepage-damage[J]. Chinese Journal of Rock Mechanics and Engineering, 2011, 30(Suppl.1): 3295–3304.

[17] ZHOU Yi, LI Shu-cai, LI Li-ping, et al. 3D fluid-solid coupled model test on water-inrush in tunnel due to seepage from filled karst conduit[J]. Chinese Journal of Rock Mechanics and Engineering, 2015, 34(9): 1739–1749.

[18] ZHOU Zong-qing. Evolutionary mechanism of water inrush through filling structures in tunnels and engineering applications[D]. Jinan: Shandong University, 2016.

[19] ZHANG Qing-yan, CHEN Wei-zhong, YUAN Jing-qiang, et al. Experimental study on evolution characteristics of water and mud inrush in fault fractured zone[J]. Rock and Soil Mechanics, 2020, 41(6): 1911–1922, 1932.

[20] ZHOU Z Q, RANJITH P G, LI S C. Optimal models for particle size distributions of granular soils[J]. Proceedings of the Institution Civil Engineers-Geotechnical Engineering, 2016, 169(1): 73–82.

[21] ZHOU Z Q, RANJITH P G, LI S C. Criteria for assessment of internal stability of granular soil[J]. Proceedings of the Institution Civil Engineers-Geotechnical Engineering, 2017, 170(1): 73–83.

[22] ZHOU Z Q, RANJITH P G, LI S C. An experimental testing apparatus for study of suffusion of granular soils in geological structures[J]. Tunnelling and Underground Space Technology, 2018, 78: 222–230.

[23] ERGUN S. Fluid flow through packed columns[J]. Chemical Engineering Progress, 1952, 48(2): 89–94.

[24] WEN C Y, YU Y H. Mechanics of fluidization[J]. Chemical Engineering Progress Symposium Series, 1966, 62: 100–111.

[25] ZHOU Zong-qing, RANJITH P G, YANG W M, et al. A new set of scaling relationships for DEM-CFD simulations of fluid–solid coupling problems in saturated and cohesiveless granular soils[J]. Computational Particle Mechanics, 2019, 6(4): 657–669.